Article

Effects of Hall Current and Thermal Radiation on the Time-Dependent Swirling Flow of Hybrid Nanofluids over a Disk Surface: A Bayesian Regularization Artificial Neural Network Approach

Faisal Nazir [1], Nirman Bhowmike [2], Muhammad Zahid [3],*, Sultan Shoaib [4],*, Yasar Amin [3] and Saleem Shahid [5]

[1] Department of Mathematical Sciences, University of Engineering and Technology, Taxila 47050, Pakistan; faisal.nazir@students.uettaxila.edu.pk
[2] Phillip M. Drayer, Department of Electrical Engineering, Lamar University, Beaumont, TX 77705, USA; nbhowmike@lamar.edu
[3] Department of Telecommunication Engineering, University of Engineering and Technology, Taxila 47050, Pakistan; yasar.amin@uettaxila.edu.pk
[4] Department of Electrical and Computer Engineering, Gulf University of Science and Technology, Hawally 32093, Kuwait
[5] Institute of Microwave and Photonic Engineering, Graz University of Technology, Inffeldgasse 12/L, 8010 Graz, Austria; saleem.shahid@tugraz.at
* Correspondence: muhammad.zahid@uettaxila.edu.pk (M.Z.); shoaib.s@gust.edu.kw (S.S.)

Abstract: For automobile and aerospace engineers, implementing Hall currents and thermal radiation in cooling systems helps increase the performance and durability of an engine. In the case of solar energy systems, the effectiveness of heat exchangers and solar collectors can be enhanced by the best use of hybrid nanofluids and the implementation of a Hall current, thermophoresis, Brownian motion, a heat source/sink, and thermal radiation in a time-dependent hybrid nanofluid flow over a disk for a Bayesian regularization ANN backpropagation algorithm. In the current physical model of Cobalt ferrite $CoFe_2O_4$ and aluminum oxide Al_2O_3 mixed with water, a new category of the nanofluid is called the hybrid nanofluid. The study uses MATLAB bvp4c to unravel such intricate relations, transforming PDEs into ODEs. This analysis enables the numerical solution of several BVPs that govern the system of the given problem. Hall currents resulting from the interaction between magnetic fields and the electrically conducting nanofluid, and thermal radiation as an energy transfer mechanism operating through absorption and emission, are central factors for controlling these fluids for use in various fields. The graphical interpretation assists in demonstrating the character of new parameters. The heat source/sink parameter is advantageous to thermal layering, but using a high Schmidt number limits the mass transfer. Additionally, a backpropagation technique with Bayesian regularization is intended for solving ordinary differential equations. Training state, performance, error histograms, and regression demonstration are used to analyze the output of the neural network. In addition to this, there is a decrease in the fluid velocity as magnetic parameter values decrease and a rise in the fluid temperature while the disk is spinning. Thermal radiation adds another level to the thermal behavior by altering how the hybrid nanofluid receives, emits, and allows heat to pass through it.

Keywords: thermophoresis and Brownian motion; heat source/sink; hybrid nanofluid; ($CoFe_2O_4$-Al_2O_3) nanoparticles; Hall current; Bayesian regularization backpropagation algorithm; rotating disk; numerical solutions

1. Introduction

Hybrid nanofluids are an improved form of thermal fluids developed by suspending two or several dissimilar nanoparticles in a basic fluid. This novel approach takes advan-

tage of the individual peculiarities of various nanoparticle types to improve the thermal characteristics and stability of the fluid. For the base fluid, water, ethylene glycol, or oils can be used and nanoparticles can be composed of metal oxides like Al_2O_3 or CuO, metals like Cu or Ag, carbon-based materials like graphene, CNTs, and other nanomaterials. The interactions between the particles can result in enhancements in thermal convergence, specific heat, and viscosity and convective heat transfer coefficients and rates better than those of base nanofluids with single nanoparticles [1,2]. One of the greatest applications is its use in cooling circuits for electronics and electric elements since controlling the temperature is important for functionality and durability [3]. New hybrid nanofluids can greatly increase the thermal conductivity of cooling systems, which means that electronics can be made smaller but more powerful [4]. In the automotive and aerospace industries, they are used in radiators and cooling systems to enhance thermal management efficiencies which, as a result, leads to more fuel efficiency and fewer emissions.

Furthermore, there is also research on the application of hybrid nanofluids in solar thermal systems [5]. Due to the enhancement of the ability of these fluids in heat transfer and absorption, the efficiency of solar collectors can be improved, which will contribute to better solutions based on renewable energy [6]. Some of the latest developments include studies that have studied how the thermal characteristics of hybrid nanofluids could be enhanced and how their viscosity, which is important in pumping and flow systems, could be kept to an acceptable level [7]. Moreover, research has been carried out on thermal properties, concentration variations, and their stability to provide the long-term stability of hybrid nanofluids. These attributes cause the nanoparticles to aggregate or sediment and thereby reduce the performance over time, so stabilization of the nanoparticles is an important area of research. Research articles, which include the current one, present extensive investigations on the use of hybrid nanofluids, accompanied by evaluation of their performance and real-life applications [8]. The future work mentioned in these studies targets continued innovation and the possibility of a hybrid nanofluid redefining thermal systems in every field.

Thermophoresis and Brownian motion are paramount processes in the investigation of particle motion in fluids of significance in nanofluids and aerosols. The Soret effect or thermophoresis is any process that leads to the migration of particles in a fluid due to a temperature gradient [9,10]. These natural occurrences make the particles travel from regions of high temperatures to regions of low temperatures and this is brought about by differential kinetic energy that is transferred to the particles by the fluid molecules at the relative temperatures of the two regions. Thermophoresis plays a monumental role in the aerosol deposition processes in thermal insulation, environmental control, etc., because it affects the movement of particulate matter [11]. In nanofluids, the thermophoresis ability may alter the stability and uniform distribution of nanoparticles, thereby affecting the fluid's thermal conductivity and heat transfer coefficients [12]. Brownian movement, on the other hand, is the irregular or random movement of small particles in a fluid due to the impact of the molecules in the fluid. This motion is more significant when the dispersed phase is made of petite particle sizes and a general reason for the dispersion and blending of nanoparticles in a fluid [13]. Brownian motion is very essential in nanotechnology and materials science when analyzing and predicting the behavior of colloidal suspensions, especially nanofluids, and is the key to the aggregation and stability of nanoparticles [14].

The concept of rotating disks is irreplaceable in numerous lines of industries and scientific research based on their flow characteristics and heat transfer behavior. Rotating disk systems that make use of centrifugal forces resulting from the rotation of the disk have a displacement in the radial sense which greatly influences heat and mass transfer [15–17]. It is used in most technologies, for example, centrifugal separators that use disks that rotate to separate particles from fluids depending on their densities. A similar application is in high-speed disk drives and data storage devices, in which rotary disks rapidly provide data access and storage data [18]. In the same way, disks that rotate are very important in chemical reactors and mixing processes since the rotation improves the mixing effi-

ciency of the reactants, thereby resulting in uniform reactions as well as superior-quality products [19]. The latest studies related to this area have targeted the enhancement of the efficiency of the rotating disk systems in as many ways as possible [20,21]. For instance, the use of new iterations in material science in conjunction with the application of surface coatings in enhancing the performance of rotating disks assembled in industrial separators and reactors has been investigated. Micro-patterned surfaces and updated coating have been several of the breakthroughs that have improved the heat transfer rates and lowered fouling [22]. The research discussed here focuses on the development of these technologies with an emphasis on the role of rotary disks in enhancing the efficiency of energy collection and transformation processes [23]. The research studies different compositions of hybrid nanofluid and investigates the influence of nanoparticle type and concentration on the thermal behavior in the rotating disk system [24,25]. Addressing the current literature, it is possible to observe that these systems are of vital importance in the processes of industry growth and energy development, as well as in the usage of data storage solutions, which testifies to their versatility and the potential for further developments.

Bayesian regularization (BR) is one advanced technique that improves ANNs by controlling the overfitting and generalization capabilities of the artificial neural networks on large and noisy data sets. This algorithm adopts the features of Bayes' theorem for the determination of the network weights where the network is adjusted to look for a solution that best balances error and model size. Unlike previous approaches such as early stopping, BR adapts the cost function by adding the regularization term, which results in the sum of the squared weights, which trades off the fit to training data for the model's smoothness [26]. Therefore, it minimizes the chance of overfitting, enables the ANN to give optimal results on unseen data, and is very applicable for computational fluid dynamics and heat transfer complications like hybrid nanofluid flow problems [27]. Because of the improved thermal and electrical conductivity characteristics of hybrid nanofluids, the appropriate mathematical representation of hybrid nanofluids is best described by nonlinear partial differential equations [28,29]. Researchers utilize Bayesian regularization in the ANN so they can interpret the complex physical behaviors of hybrid nanofluids while avoiding overfitting noisy or lacking data to the network [30]. This approach is especially helpful in the description of time-variable swirling flows, in which additional dynamic parameters such as the Hall current and thermal radiation also play a pivotal role.

The current study aims to give an extensive evaluation of the different approaches to an unstable $CoFe_2O_4$-Al_2O_3 and water flow under the influence of a spinning disk in line with the literature reviews above. The model equations are numerically solved, and the results are analyzed and validated by comparing them with the results of the MATLAB bvp4c tool. The training state, performance, error histograms, and regression demonstration of the ternary hybrid nanofluid are analyzed using the Bayesian regularization backpropagation algorithm.

2. Problem Formulation

In the present study, an unsteady MHD hybrid nanofluid flow over a stretched rotating disk is examined under the effects of a Hall current, heat source/sink, and thermal radiation. The $CoFe_2O_4$ and Al_2O_3 are the two varieties of nanoparticles in the flow. For the problem under consideration, we adopt the cylindrical coordinate system r, ϕ, z. The disk itself rotates at an angular velocity Ω about the z-axis in the configuration when $z = 0$. In the direction of the z-axis, there is always employed a uniform magnetic field, which is referred to as B_0, as shown in Figure 1. The surface temperature of the disk is labeled T_s, while the temperature outside the disk is labeled T_0. Thick disk stretching velocities, the thickness of the plane, and the temperature gradient are all time and space varying, like the rotational velocities of the disk. The following assumptions are made to simplify the problem:

$$u = \frac{cr}{(1 - bt)}, v = \frac{r\Omega}{(1 - bt)}, B(t) = \frac{B_0}{(1 - bt)^{\frac{1}{2}}}, T_s = T_0 - T_{ref} \frac{r^2 \Omega}{v_f (1 - bt)^{\frac{3}{2}}}. \tag{1}$$

An appropriate magnetic field is assumed to induce the Hall current [31]. The generalized Ohm's law follows this approach when there is an electric field:

$$\mathbf{J} + \frac{\omega_e \tau_e}{B_0} (\mathbf{J} \times \mathbf{B}) = \sigma [\mu_e \mathbf{V} \times \mathbf{B} + \frac{1}{en_e} \nabla p_e], \tag{2}$$
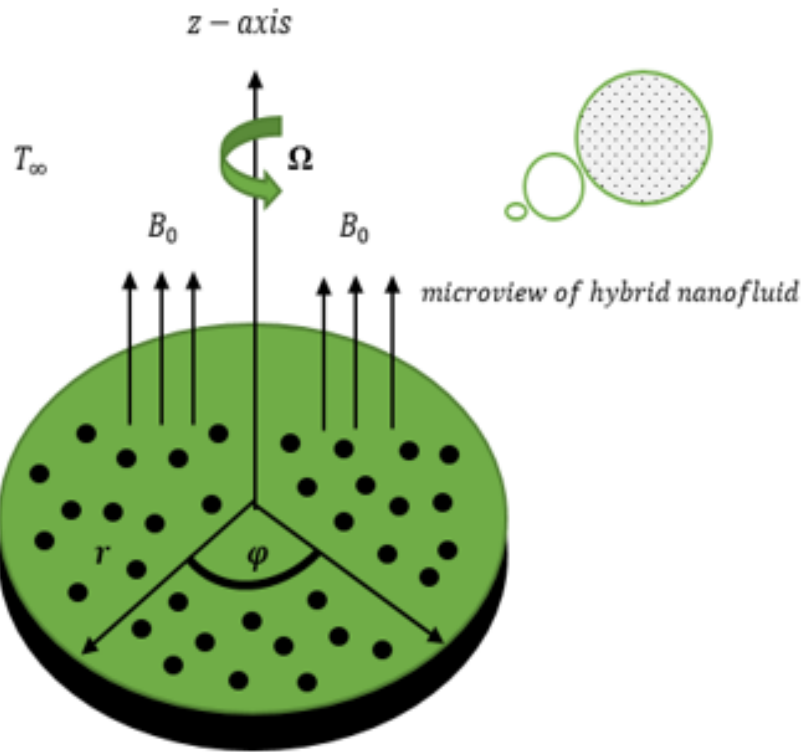
Figure 1. Flow configuration.

Assuming that the ion slip and thermoelectric pressure requirements for weakly ionized gas are insignificant, the above equations are reduced to the following form:

$$J_r = \frac{\sigma \mu_e B_0}{1 + m^2} (mv - u), J_\phi = \frac{\sigma \mu_e B_0}{1 + m^2} (mu + v) \tag{3}$$

where $\Omega, b, c, T_0, T_s, T_{ref}, \omega_e, p_e, \tau_e, \mu_e, n_e, m, B_0, \sigma, u, v$ stand for the disk rotating rate, positive constant, stretching rate, original temperature, surface temperature, constant reference temperature, cyclotron frequency of electrons, constant reference temperature, electron pressure, electron collision time, and magnetic parameter. Here, the electrical conductivity of the fluid is $\sigma = \left(\frac{e^2 n_e t_e)}{m_e}\right)$, and the Hall parameter is defined as $m = (\omega_e \tau_e)$. In the stated expectations, the governing equations are (Refs. [32,33]) as follows:

$$\frac{\partial w}{\partial z} + \frac{1}{r} \frac{\partial}{\partial r} (ur) = 0 \tag{4}$$

$$\frac{\partial u}{\partial t} - \frac{v^2}{r} + w \frac{\partial u}{\partial z} + u \frac{\partial u}{\partial r} = v_{hnf} \left(\frac{\partial^2 u}{\partial z^2}\right) - \frac{\sigma_{hnf} B_0^2}{\rho_{hnf} (1 + m^2)(1 - bt)} (u - mv), \tag{5}$$

$$\frac{\partial v}{\partial t} + \frac{uv}{r} + w\frac{\partial v}{\partial z} + u\frac{\partial v}{\partial r} = \nu_{hnf}\left(\frac{\partial^2 v}{\partial z^2}\right) - \frac{\sigma_{hnf}B_0^2}{\rho_{hnf}(1+m^2)(1-bt)}(v+mu), \tag{6}$$

$$\frac{\partial T}{\partial t} + w\frac{\partial T}{\partial z} + u\frac{\partial T}{\partial r} = \frac{k_{hnf}}{(\rho C_p)_{hnf}}\left(\frac{\partial^2 T}{\partial z^2}\right) - \tau\left(\frac{\partial T}{\partial z}\frac{\partial C}{\partial z} + \frac{D_T}{T_0}\frac{\partial^2 T}{\partial z^2}\right) + \frac{\mu_{hnf}}{(\rho C_p)_{hnf}}\left[\left(\frac{\partial u}{\partial z}\right)^2 + \left(\frac{\partial v}{\partial z}\right)^2\right] - \frac{1}{(\rho C_p)_{hnf}}\frac{\partial}{\partial z}(q_r) + \frac{Q_0(T-T_s)}{(\rho C_p)_{hnf}}, \tag{7}$$

$$\frac{\partial C}{\partial t} + w\frac{\partial C}{\partial z} + u\frac{\partial C}{\partial r} = D_B\left(\frac{\partial^2 C}{\partial z^2}\right) + \left(\frac{D_T}{T_0}\frac{\partial^2 T}{\partial z^2}\right) \tag{8}$$

where $\rho_{hnf}, \sigma_{hnf}, \nu_{hnf}, k_{hnf}, (\rho C_p)_{hnf}, q_r, C, T, D_T, D_B, \tau$ are the density of the hybrid nanofluid, hybrid nanofluid electrical conducting, kinematic viscosity, thermal conductivity of the hybrid nanofluid, fluid concentration of the hybrid nanofluid, radiative heat flux, specific heat of the hybrid nanofluid, fluid temperature, thermophoresis diffusion coefficient, Brownian diffusion coefficient, and heat capacities ratio of the hybrid nanofluid, respectively. The Rosseland approximation can be used to express the radiative heat flux in this case as follows:

$$q_r = -\frac{4\sigma^*}{3k^*}\frac{\partial T^4}{\partial z} = -\frac{16\sigma^* T_0^3}{3k^*}\left(\frac{\partial T}{\partial z}\right), \tag{9}$$

Because of Equations (7) and (8) can be expressed with BCs:

$$u = \frac{cr}{(1-bt)}, v = \frac{r\Omega}{(1-bt)}, w = 0, T = T_s, C = C_s, at\, z = 0, \tag{10}$$

$$\frac{\partial u}{\partial z} = 0, \frac{\partial v}{\partial z} = 0, \frac{\partial T}{\partial z} = 0, \frac{\partial C}{\partial z} = 0, at\, z \to \infty, \tag{11}$$

Consider the following similarity transformations:

$$u = \frac{cr}{(1-bt)}f'(\eta), v = \frac{r\Omega}{(1-bt)}g(\eta), w = -2\left(\frac{\nu_f\Omega}{1-bt}\right)^{\frac{1}{2}},$$

$$T = T_0 - T_{ref}\frac{r^2\Omega}{\nu_f(1-bt)^{\frac{3}{2}}}\theta(\eta), C = C_0 - C_{ref}\frac{r^2\Omega}{\nu_f(1-bt)^{\frac{3}{2}}}\phi(\eta), \eta = \sqrt{\frac{\Omega}{\nu_f(1-bt)}}z. \tag{12}$$

Equations (4)–(8), (10) and (11) are reduced to

$$\left(\frac{A_1}{A_2}\right)f''' + (g^2 + 2ff' - f'^2) - S\left(\frac{\eta}{2}f'' + f'\right) - \frac{A_3}{A_2(1+m^2)}M(f' - mg) = 0, \tag{13}$$

$$\left(\frac{A_1}{A_2}\right)g'' - S\left(\frac{\eta}{2}g' + g\right) - 2(fg' + f'g) - \frac{A_3}{A_2(1+m^2)}M(g - mf') = 0, \tag{14}$$

$$A_4\left(A_5 + \frac{4}{3}R_d\right)\theta'' - PrS\left(\frac{\eta}{2}\theta' + \frac{3}{2}\theta\right) + 2Pr(f\theta' - f'\theta) - \frac{A_4}{A_1}PrEc\left(f''^2 + g'^2\right) + PrQ_E\theta + Pr\left(Nt\theta'^2\right) + Nb\theta'\phi' = 0, \tag{15}$$

$$\phi'' + 2Sc(f\phi' - f'\phi) - \frac{1}{2}Sc(3\phi + \eta\phi')S + \frac{Nt}{Nb}\theta'' = 0, \tag{16}$$

with conditions

$$f'(0) = \omega, f(0) = 1, g(0) = 1, \theta(0) = 1, \phi(0) = 1, at\, \eta = 0, \tag{17}$$

$$f''(\infty) = 0, g'(\infty) = 0, \theta'(\infty) = 0, \phi'(\infty) = 0, as\, \eta \to \infty. \tag{18}$$

where $w, \omega, S, Rd, M, Pr, Ec, Q_E$ are the rotation variable, Hall current parameter, Eckert number, measure of unsteadiness, radiation variable, magnetic field number, Prandtl

number, heat source number, slip variable, and Biot number, respectively. These mathematical forms and dimensionless parameters of constants A_1, A_2, A_3, A_4, A_5 can be expressed as follows:

$$
\begin{aligned}
&w = \omega_e \tau_e, \omega = \frac{\Omega}{c}, S = \frac{b}{\Omega}, \\
&Rd = \frac{4\sigma^* T_\infty^3}{k^* k_f}, M = \frac{\sigma_f B_0^2}{\rho_f \Omega}, Pr = \frac{\mu_f(\rho Cp)_f}{\rho_f k_f}, Q_E = \frac{Q_0(1 - bt)}{(\rho Cp)_f \Omega}, \\
&Ec = \frac{r^2 \Omega^2}{(T_0 - T_s)(1 - bt)^2}, Nt = \frac{\tau D_T(T_0 - T_s)}{T_0 \nu_f}, Nb = \frac{\tau D_B(C_0 - C_s)}{\nu_f}, Sc = \frac{\nu_f}{D_B}, \\
&A_1 = \frac{\mu_{hnf}}{\mu_f}, A_2 = \frac{\rho_{hnf}}{\rho_f}, A_3 = \frac{\sigma_{hnf}}{\sigma_f}, A_4 = \frac{(\rho Cp)_{hnf}}{(\rho Cp)_f}, A_5 = \frac{k_{hnf}}{k_f}
\end{aligned}
\tag{19}
$$

The local Nusselt numbers Nur [34] and the local Sherwood number Shr [35] are defined as

$$
Nu_r = -\left(1 + \frac{16\sigma^* T_0^3}{3kk^*}\right) \frac{r(\frac{\partial T}{\partial z})_{z=0}}{k_{hnf}(T_s - T_0)},
\tag{20}
$$

$$
Sh_r = -\frac{r(\frac{\partial C}{\partial z})_{z=0}}{k_{hnf}(C_s - C_0)},
\tag{21}
$$

where q_w denotes the heat flux. The dimensionless forms are

$$
Re^{-\frac{1}{2}} Nu_r = -\left(\frac{k_{hnf}}{k_f}\right)\left(1 + \frac{4}{3}Rd\right)\theta(0),
\tag{22}
$$

$$
Re^{-\frac{1}{2}} Sh_r = -\phi'(0),
\tag{23}
$$

where $Re^{\frac{1}{2}} = r\sqrt{\frac{\Omega}{\nu_f(1 - bt)}}$ is the local Reynold parameter.

3. Hybrid Nanofluid Model

The various flow illustrations say that the $\rho_{hnf}, \mu_{hnf}, k_{hnf}, (\rho Cp)_{hnf}$ of $CoFe_2O_4$-Al_2O_3 and water are defined as

$$
\mu_{hnf} = \mu_{bf}(1 - \phi_{np1})^{-2.5}(1 - \phi_{np2})^{-2.5}
\tag{24}
$$

$$
\rho_{hnf} = (1 - \phi_{np2})[(1 - \phi_{np1})\rho_{bf} + \phi_{np1}\rho_{np1}] + \phi_{np2}\rho_{np2}
\tag{25}
$$

$$
(\rho Cp)_{hnf} = (1 - \phi_{np2})[(1 - \phi_{np1})(\rho Cp)_{bf} + \phi_{np1}(\rho Cp)_{np1} + \rho_{np2}(\rho Cp)_{np2}]
\tag{26}
$$

$$
\sigma_{hnf} = \frac{\sigma_{np2} + 2\sigma_{nf} - 2\phi_{np2}(\sigma_{nf} - \sigma_{np2})}{\sigma_{np2} + 2\sigma_{nf} + \phi_{np2}(\sigma_{nf} - \sigma_{np2})}\sigma_{nf}
\tag{27}
$$

where

$$
\sigma_{nf} = \frac{\sigma_{np1} + 2\sigma_{bf} - 2\phi_{np1}(\sigma_{bf} - \sigma_{np1})}{\sigma_{np1} + 2\sigma_{bf} + \phi_{np1}(\sigma_{bf} - \sigma_{np1})}\sigma_b f
\tag{28}
$$

$$
k_{hnf} = \frac{k_{np2} + (s-1)k_{nf} - (s-1)\phi_n p2(k_{nf} - k_{np2})}{k_{np2} + (s-1)k_{nf} + \phi_{np2}(k_{nf} - k_{np2})}k_{nf}
\tag{29}
$$

where

$$
k_{nf} = \frac{k_{np1} + (s-1)k_{bf} - (s-1)\phi_{np1}(k_{bf} - k_{np1})}{k_{np1} + (s-1)k_{bf} + \phi_{np1}(k_{bf} - k_{np1})}k_{bf}
\tag{30}
$$

Here, index $np1$ and $np2$ represent the nanoparticles of Cobalt Ferrite $CoFe_2O_4$ and aluminum oxide Al_2O_3, whereas bf, nf, and hnf define the base fluid, nanoliquid, and

hybrid nanoliquid. The solid volume fraction for ϕ_{np1} and ϕ_{np2} of $CoFe_2O_4$-Al_2O_3 and water is taken as fixed in the present study. Table 1 shows the numerical values for various thermal parameters for the base fluid and the nanoparticles.

Here, index $np1$ and $np2$ represent the nanoparticles of Cobalt Ferrite $CoFe_2O_4$ and aluminum oxide Al_2O_3, while bf, nf, and hnf denote the base fluid, nanoliquid, and hybrid nanoliquid. In the present analysis, the solid volume fraction for both ϕ_{np1} and ϕ_{np2} of $CoFe_2O_4$-Al_2O_3 as well as water is chosen as constant. The numerical values for the different thermal parameters of the base fluid and the nanoparticles are presented in Table 1.

Table 1. Physical properties of nano-addictive base fluid [36,37].

	ρ (kg/m^3)	k (W/mk)	Cp (J/kgk)	σ (S/m)$^{-1}$
Pure water	997.1	0.613	4197	0.05
$CoFe_2O_4$	4908	3.6	700	1.1×10^7
Al_2O_3	3970	40	765	35×10^{-6}

4. Numerical Solution

In the present section, the procedure for the numerical integration of temperature equations and dimensionless nonlinear momentum is explained. Using one of the above-mentioned collection methods, the bvp4c technique that uses the Lobatto IIIA formula, Equations (13)–(17) are solved numerically. This method also has its boundary conditions that need to be fulfilled to arrive at the above-noted results. Subsequently, a totally different method, which is known as finite difference, is used to adjust the initial guess that was made earlier for further iterations. To apply this method, it is necessary to reduce the problem into a system of first-order ODEs. We take the following actions to achieve this:

$$
\begin{aligned}
f &= F_1, f' = F_2, f'' = F_3, f''' = FF_1, \\
g &= F_4, g' = F_5, g'' = FF_2, \\
\theta &= F_6, \theta' = F_7, \theta'' = FF_3, \\
\phi &= F_8, \phi' = F_9, \phi'' = FF_4,
\end{aligned}
\tag{31}
$$

$$
FF_1 = \frac{SA_2}{A_1}\left(\frac{\eta}{2}F_3 + F_2\right) - \frac{A_2}{A_1}(F_4^2 + 2F_1F_3 - F_2^2) + \frac{A_3}{A_1}(1 + m^2)M(F_2 - mF_4),
\tag{32}
$$

$$
FF_2 = \frac{SA_2}{A_1}\left(\frac{\eta}{2}F_5 + F_4\right) - \frac{2A_2}{A_1}(F_1F_5 - F_2F_4) + \frac{A_3}{A_1}(1 + m^2)M(F_4 - mF_2),
\tag{33}
$$

$$
FF_3 = \left(\frac{PrS}{A_4}\left(\frac{\eta}{2}F_7 + \frac{3}{2}F_6\right) - \frac{2Pr}{A_4}(F_1F_7 - F_2F_6) + \frac{PrEc}{A_1}(F_3^2 + F_5^2) + Pr(NtF_7^2 + NbF_7F_9) - PrQ_EF_6\right)/\left(A_5 + \frac{4}{3}Rd\right),
\tag{34}
$$

$$
FF_4 = -2Sc(F_1F_9 - F_2F_8) + \frac{1}{2}Sc(3F_8 + \eta F_9)S - \frac{Nt}{Nb}FF_3,
\tag{35}
$$

with conditions

$$
F_1(0) = 0, F_2(0) = \omega, F_4(0) = 1, F_6(0) = 1, F_8(0) = 1,
\tag{36}
$$

$$
F_3(\infty) = 0, F_5(\infty) = 0, F_7(\infty) = 0, F_9(\infty) = 0.
\tag{37}
$$

5. Intelligent Computing: ANN-BR Scheme

There are two basic forms of training neural networks: supervised and unsupervised, where, as in the case of unsupervised learning, the neural network is on its own trying to decipher perceived input values. However, in this study, supervised learning is used, in which the input and output values are given to the network. The network then takes the input data passed into the network and transforms them to produce an output that is

compared with the target outputs. The system then uses the method of error propagation to correct the weights that govern the neural network for further tuning. Moreover, the classic form of modeling such complex fluid flows can be a problem as it demands solving complex parabolic equations regarding the substance. ANNs can be thought of as an alternative as they allow the modeling of nonlinear variables even if we do not know their equations. Though they have an impressive capability to learn the relationships within the data, ANNs are prone to overfitting, whereby the model learns from the training data set with excessive finesse and thus has low chances of correctly predicting unknown data sets. This can be solved by applying a BRS for the training of the ANNs; this allows for the embedding of preexisting data about the model parameters into the model and reduces overfitting. In the training of the weights of networks, the Bayesian regularization scheme (BRS) is employed. A brief overview of the BRS is as follows: According to a report, BRS-optimized networks are said to be stable, reliable, and more accurate than the networks used in supervised-learning-based backpropagation [38]. The BRS works under the L-M method without cross-validation checks being performed on the validation samples in the weight-tuning procedures. In the case of the BRS, what is applied is a nonlinear regression. The mathematical procedure it is based on is then transformed/substituted into an equivalent statistical optimization problem by the use of ridge regression. For detailed information about the BRS in terms of subject terms, mathematical theory, and theoretical convergence proof, interested readers are referred to [39].

For the purpose of implementing the proposed ANN-BRS, the routine called "nftool" in MATLAB is used, and, for the weight training of the neural network, the BRS is applied. As per the normal execution of the "nftool" routine, efficient backpropagation is performed via L-M methods, which usually consider a training/testing/validation sample grid of targets and inputs to reasonably accurately/efficiently train the networks; however, the adaptive L-M procedure is known to be challenged by validation checks, which may lead to the issue of premature convergence, namely, a lack of accuracy or instability for the majority of multiple stiff modeling cases. Nonetheless, the use of the proposed ANN-BR scheme means that the Bayesian distribution-based statistical procedure is used to overcome or eliminate the validation checks which may arise in the validation process of the L-M methodology but, at the same time, are subject to relatively more computations in the BRS. However, noting these facts, the best compromise is struck when there is a trade off between accuracy and complexity in the suggested ANN-BR scheme.

6. Discussion of Results

A variation in the volume concentration of nanoparticles for $f'(\eta)$ and $g(\eta)$ is demonstrated in Figure 2a,b. This study particularly shows that, when the volume volumetric concentration of the hybrid nanofluid is raised, the thermal boundary layer becomes thicker, which results in an upsurge in $f'(\eta)$. On the other hand, as the volume percentage of the hybrid nanofluid rises, the azimuthal velocity $g(\eta)$ rises. The variation in the temperature profile with the volume fraction of ϕ_1 is depicted in Figure 2c. This is shown to induce a progressive variation of ϕ_1 that decays the temperature field. The first reason is because nanoparticle incorporation increases the thermal conductivity of fluids, which, in return, enhances fluid temperature. Figure 3a–c amplify further the velocity profiles and thermal profile against the Hall current m. The features are made clear by both velocity fields in Figure 3a,b, which show that both the velocity fields are enhanced by the act of the Hall current m. A presentation of the energy profile against the Hall current difference is presented in Figure 3c. It elucidates that the thermal profile is augmented by the positive-disparity Hall current m. As in the case of a Hall current, it also gives rise to resistance, which improves the thermal performance of the fluid flow, as plotted in Figure 3c. Figure 4a,b delineate the comparative of the magnetic parameter M on axial velocity $f'(\eta)$ and swirl velocity field $g(\eta)$. Shown in Figure 4a is the nature of M versus axial velocity field $f'(\eta)$. Lorentz forces, a variation in Lorentz forces, or an increase in resistivity cause the rate at which the fluid flows to reduce. Similar diminishing patterns are seen for improving the

value of M with thinner boundary layers in the variations of the swirl velocity $g(\eta)$ given in Figure 4b. The fact that resistance to the swirl can be linked to the fact that the magnetic field is induced in the swirl direction shows that it directly opposes the improvement of $g(\eta)$. Thus, it follows that the boundary layer is thinned in this zone and $g(\eta)$ decreases.
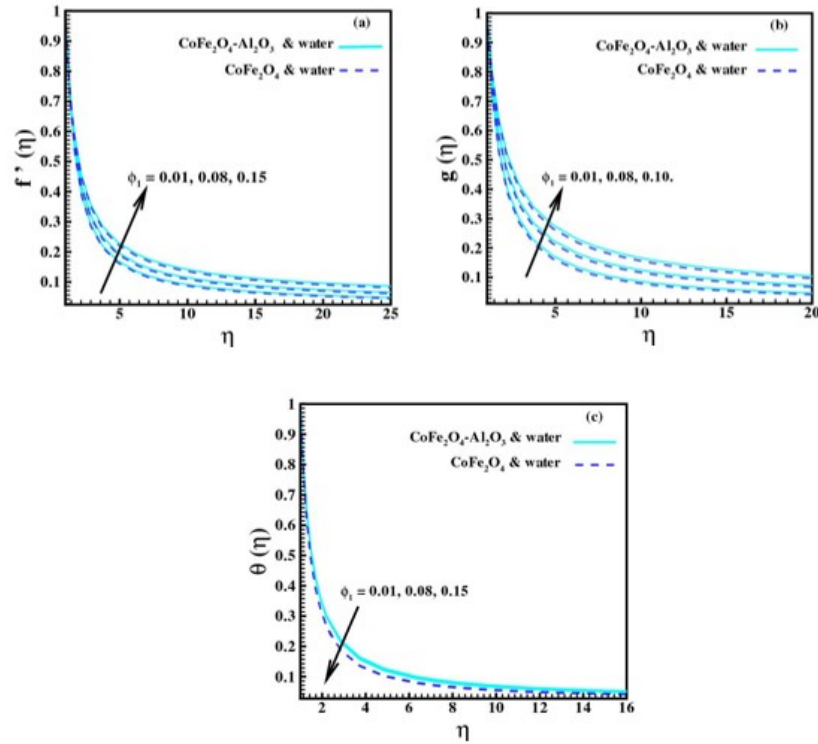
Figure 2. (**a**–**c**) Impact of ϕ_1 on $f'(\eta), g(\eta)$, and $\theta(\eta)$.
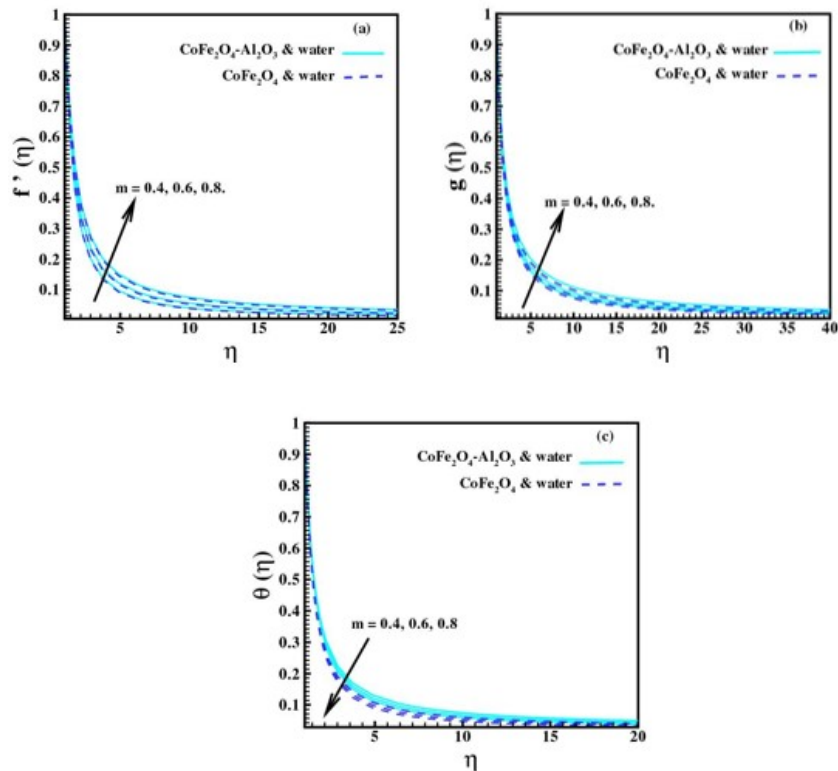
Figure 3. (**a**–**c**) Impact of m on $f'(\eta), g(\eta)$, and $\theta(\eta)$.
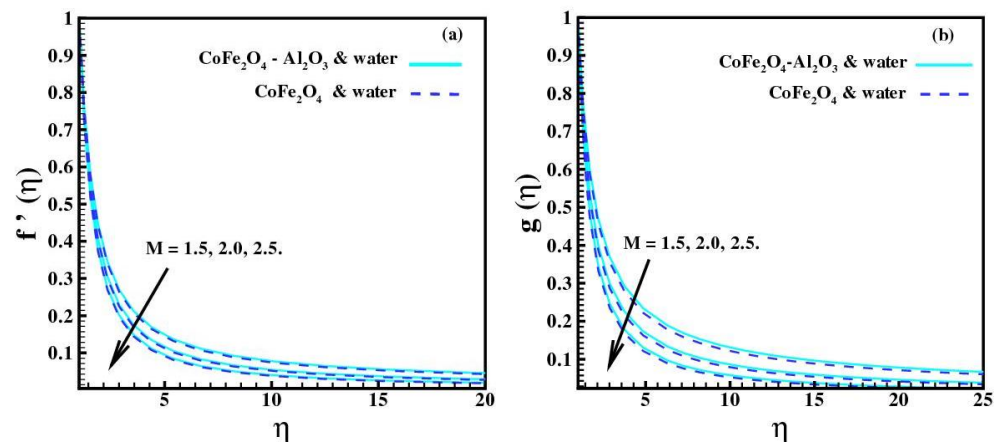
Figure 4. (**a**,**b**) Impact of M on $f'(\eta)$ and $g(\eta)$.

Figure 5a–c reveal the dependencies of $f'(\eta), g(\eta)$, and $\theta(\eta)$ on the rotation number ω. Therefore, it cannot be clearer that, in the event of the enhancement of angular velocity, the high rotation rate results in increased abstraction, and, in addition, the rotation rate increases contrary to the quantity of stretching. Plots of the radial velocity of $f'(\eta)$ as influenced by ω are presented in Figure 5a. As far as the physical meaning of an increase in the rotational number is concerned, the centrifugal force rises and acts on fluid, pressuring it and accelerating the fluid particles in the radial direction at a faster rate. In a like manner, Figure 5b shows the effect of rotation variable ω on $g(\eta)$, whereby increasing ω enhances the plot of the cross-radial velocity. In Figure 5c, the effects of ω on $\theta(\eta)$ are depicted. The documentaries prove that the increasing value of the rotation rate results in a decrease in temperature in the hybrid nanofluid.
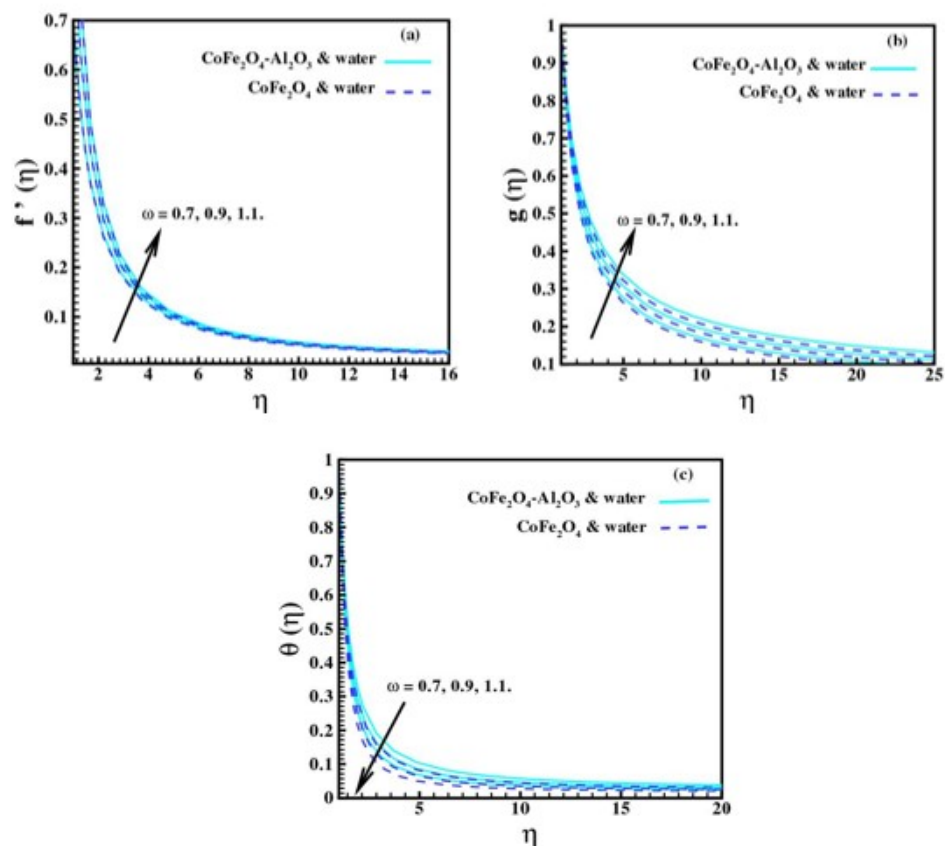
Figure 5. (**a**–**c**) Impact of ω on $f'(\eta)$, $g(\eta)$, and $\theta(\eta)$.

Figure 6a,b show the temperature and concentration outline obtained when investigating the impact of the Brownian motion factor. From the experimental data analysis, it can be seen that the increase in the Nb value leads to an increase in the concentration and temperature of the nanoparticles. Brownian motion is the erratic and chaotic movement of nanoscale particles that are dispersed within a medium and can be ascribed to sample and seal collisions. It is noticed that, when the thermophoretic effect increases, the Brownian motion also increases the temperature due to more kinetic energy. The temperature and concentration outlines of nanoparticles relative to the thermophoresis factor Nt are presented in Figure 7a,b. In Figure 3, it can be seen that, with the increase in the value of Nt, the temperature is high and the concentration profile is low. When it comes to heat transfers, it has factors in the transportation system, and one of those factors is the thermophoresis factor. This phenomenon leads to the migration of the particles from the high-temperature zone to the low-temperature zone, increasing both the temperature and the thickness of the boundary layer.
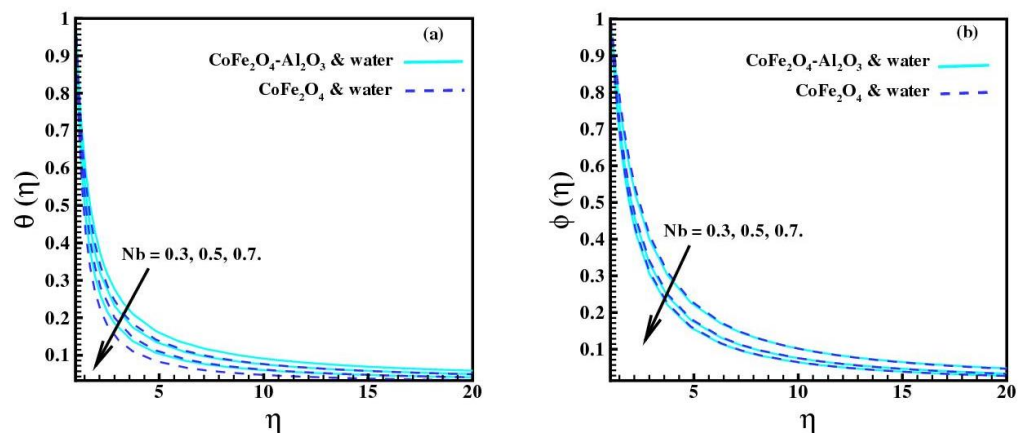
Figure 6. (**a**,**b**) Impact of Nb on $\theta(\eta)$ and $\phi(\eta)$.
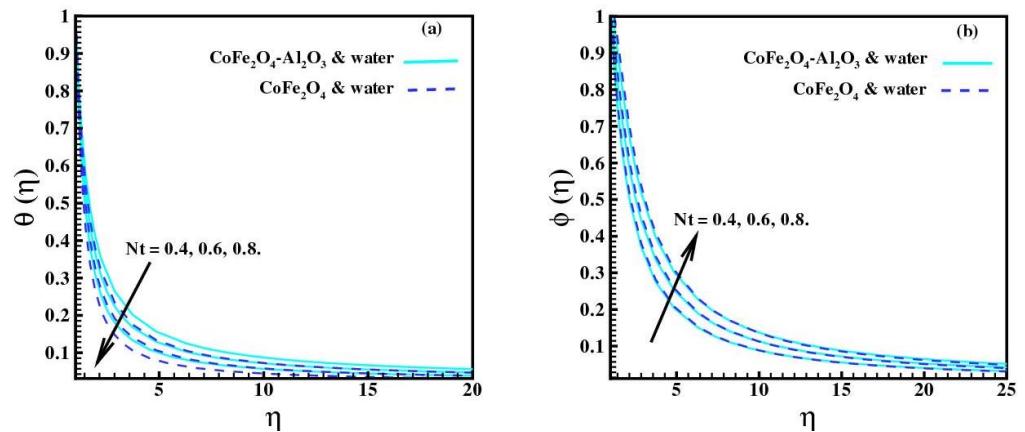
Figure 7. (**a**,**b**) Impact of Nt on $\theta(\eta)$ and $\phi(\eta)$.

The projected change in behavior concerning the thermal profile due to the Ec increase is shown in Figure 8a. From this graph, it is clear that the variation in the nanoliquid thermal profile reduces with the rising Ec values. Due to the higher viscosity of the liquid, the viscous force takes control of the boundary layer and gives rise to frictional heating within the boundary layer from a physical point of view. From this observation, it is possible to deduce that the temperature of the fluid is directly proportional to Eckert's number. Therefore, as the value of Ec rises, the nanoliquid thermal profile reduces. Details of the Prandtl number's effect on the temperature distribution are shown in Figure 8b. This means that, as greater values of the Prandtl number Pr are taken, the value of the temperature distribution of the fluid flow is decreased. The thermal profile distribution

of the fluid which is affected by *Rd* is shown in Figure 8c. It is observed that all the *Rd* boosting parameters raise the thermal profile, as given below. The proportion of heat transfer conduction to the heat transfer by thermal radiation is referred to as thermal radiation. The primary mode of heat exchange used in the operation of heat pipes is conduction, as opposed to thermal conduction. The thermal radiation parameter values rise, and hence they raise the fluid temperature and the thermal boundary layer thickness magnitude. Figure 8d shows the change in the fluid concentration due to *Sc*. It is employed to study the decrease in the role of the fluid concentration for a larger *c*. Moreover, there is a promotion in the mass transfer due to the rise in *Sc* while the thickness of the solutal boundary layer declines. Therefore, as *Sc* increases, the liquid concentration decreases.
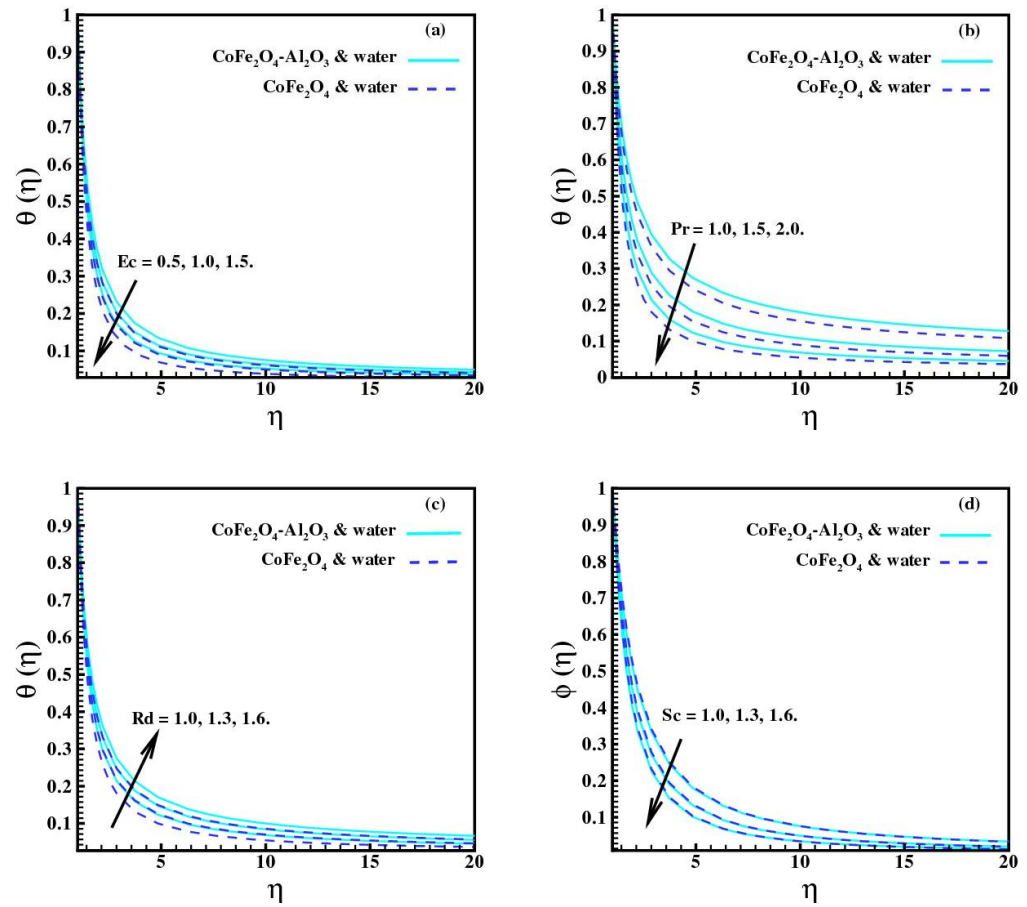
Figure 8. (**a–d**) Impact of *Ec*, *Pr*, and *Rd* on $\theta(\eta)$ and *Sc* on $\phi(\eta)$.

To obtain the influence of the various physical parameters on the local Nusselt number for both the hybrid nanofluid (HNF) and nanofluid (NF), mathematical results are attained for $Pr = 1.0, S = 0.8, Rd = 1.0, Ec = 0.5, Q_E = 0.02, \omega = 0.4, Nb = 0.5$, and $Nt = 0.2$ and are enumerated in Table 2. It shows that the Nusselt number rises with an increase in all parameters. To obtain the impact of the various physical parameters on the local Sherwood parameter with both the hybrid nanofluid and nanofluid, mathematical results are attained for $Pr = 1.0, S = 0.7, Rd = 1.0, Ec = 0.5, Q_E = 0.02, \omega = 0.4, Nb = 0.5$, and $Nt = 0.7$ and are enumerated in Table 3. It shows that the Sherwood number rises with increasing Schmidt number Sc, unsteadiness parameter S, rotation variable ω, and Brownian number Nb, while the Sherwood number decreases with an increase in the thermophoresis parameter Nt.

Table 2. Nu_r for various values of emerging variables such as $M = 2.0, m = 0.5, Sc = 0.2, \phi_1 = \phi_2 = 0.02$.

P_r	S	Rd	Ec	Q_E	Nb	ω	Nt	Nu (NF)	Nu (HNF)
0.6	0.8	1.0	0.5	0.02	0.5	0.4	0.2	1.622040	2.253789
0.8								1.938445	2.693621
1.0								2.225704	3.090755
1.0	0.3							1.780332	2.444007
	0.4							1.885911	2.599171
	0.5							1.980055	2.736396
	0.8	0.7						2.084430	2.817053
		0.8						2.133092	2.912269
		0.9						2.180144	3.003371
		1.0	0.1					2.003443	2.796124
			0.2					2.047613	2.847932
			0.3					2.091787	2.899743
			0.5	0.03				2.167230	2.984875
				0.05				2.141414	2.947895
				0.07				2.115612	2.910932
				0.01	0.6			2.203083	3.031185
					0.8			2.249686	3.087599
					1.0			2.297263	3.145064
					0.5	0.7		2.466676	3.381189
						0.9		2.686264	3.666367
						1.1		2.933866	3.984960
						0.4	0.5	2.229809	3.060558
							0.7	2.263984	3.099753
							0.9	2.299029	3.139820

Table 3. Sh_r for various values of emerging variables such as $M = 2.0, m = 0.5, Pr = Rd = 1, Ec = 0.5, Q_E = 0.02, \phi_1 = \phi_2 = 0.02$.

S_c	S	Nb	ω	Nt	Nu (NF)	Nu (HNF)
1.5	0.7	0.5	0.4	0.7	1.605421	1.940375
1.7					1.820324	2.149919
1.9					2.017342	2.341895
1.5	0.4				1.509153	1.833637
	0.5				1.543047	1.870739
	0.6				1.575134	1.906338
	0.7	0.7			1.937827	2.201451
		0.9			2.119779	2.344831
		1.1			2.233280	2.434675
		0.5	0.6		1.774717	2.151670
			0.7		1.842365	2.242591
			0.8		1.898369	2.323622
			0.4	0.2	2.650721	2.740184
				0.4	2.255309	2.434796
				0.6	1.830026	2.110249

Results with Discussion of ANN-BRS Illustrative Outcomes

The numerical simulation needed for the ANN-BRS is then used for convective flow dynamics involving the hybrid nanofluid model given by Equations (13)–(18). In the following technique, the ANN-BRS is applied to the parameters of the hybrid nanofluid model formulation. Visual representations of the best training performance convergence at different stages of the proposed model development are shown in Figure 9a–d. According to these figures, the fluid model performs best at epochs 1000, 245, 1000, and 1000, which are, for cases 1–4, associated with $4.1201 \times 10^{-6}, 2.6825 \times 10^{-1}, 8.3653 \times 10^{-4}$, and 3.1663×10^{-5}, respectively. The transitional state required to solve the modeled problem using the structure of an ANN is depicted in Figure 3a–d. These diagrams offer a visual representation of the dynamic process as the model solves problems at different phases. In these figures, the gradient values are connected with $3.8532 \times 10^{-3}, 7.552 \times 10^{-3}, 3.1364 \times 10^{-3}$, and 1.9459×10^{-1} for cases 1–4. Figure 10a has gradient information with a value of 1.3996×10^{-2}, Mu with a value of 50, and a sum square and Num parameter of 35.0944 and 26.8682, respectively, at epoch 1000. Figure 10b has gradient information with a value of 8.6865×10^{-2}, Mu with a value of 50,000,000,000.0001, and a sum square and Num parameter of 7.0401 and 11.4182, respectively, at epoch 245. Figure 10c has gradient information with value 3.2655×10^{-3}, Mu with value 5, and a sum square and Num parameter of 19.1884 and 24.015, respectively, at epoch 1000. Figure 10a has gradient information with a value of 2.9538×10^{-2}, Mu with value 5, and a sum square and Num parameter of 36.0363 and 33.8784, respectively, at epoch 1000. The suggested model's regression performance

for cases 1–4 is shown in Figure 11a–d. A consistent pattern emerges from a study of all the images, showing that, for the training, testing, and validation data sets, the correlation values indicated by the letter "R" cluster closely around unity. An essential finding is that the ANN design for the suggested model is highly precise, as evidenced by its closeness to unity. The error histogram for the suggested model is shown in Figure 12a–d. Based on these figures, it can be observed that the estimated values for cases 1–4 are related to -0.3426, -0.1369, 0.08825, and 0.06399. The suggested fluid flow model's convergence and precision are demonstrated visually in these diagrams (Figure 12a–d) and Figure 13.

(a)

(b)

(c)

(d)
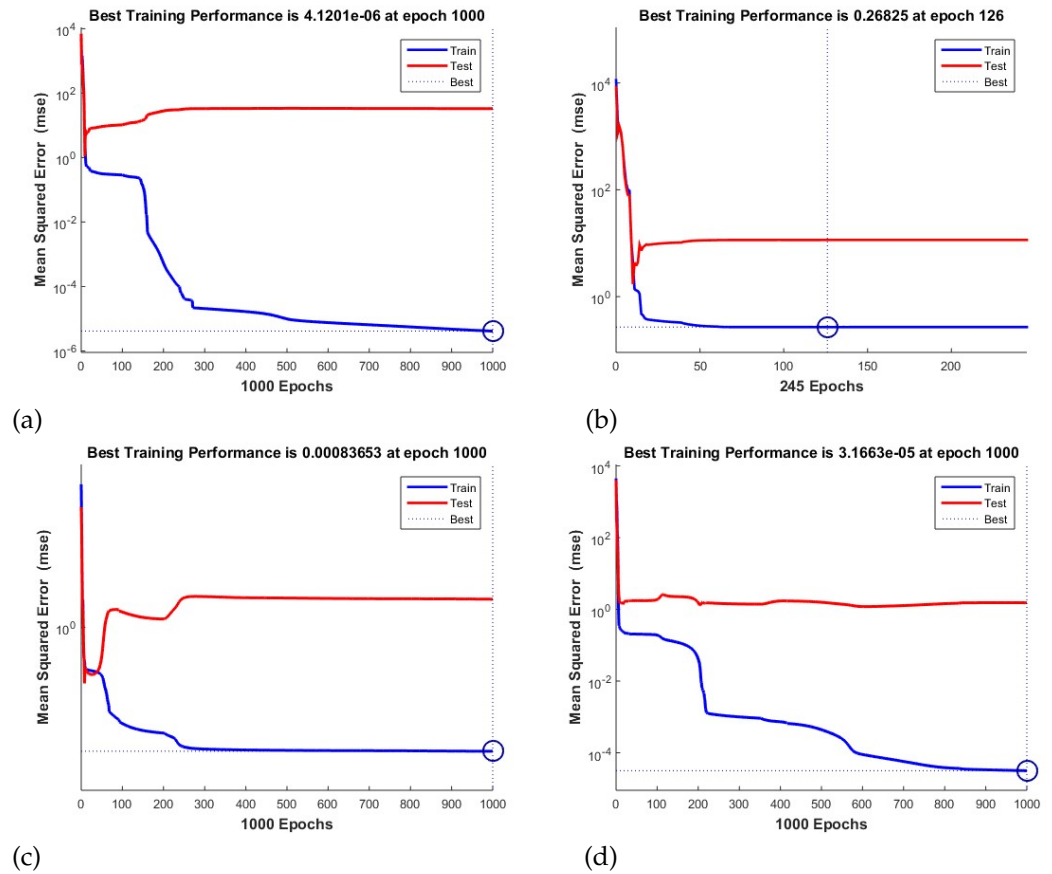
Figure 9. (**a**–**d**) Graphical view for illustration of best training performance for ANN-BR outcomes.

(a)

(b)
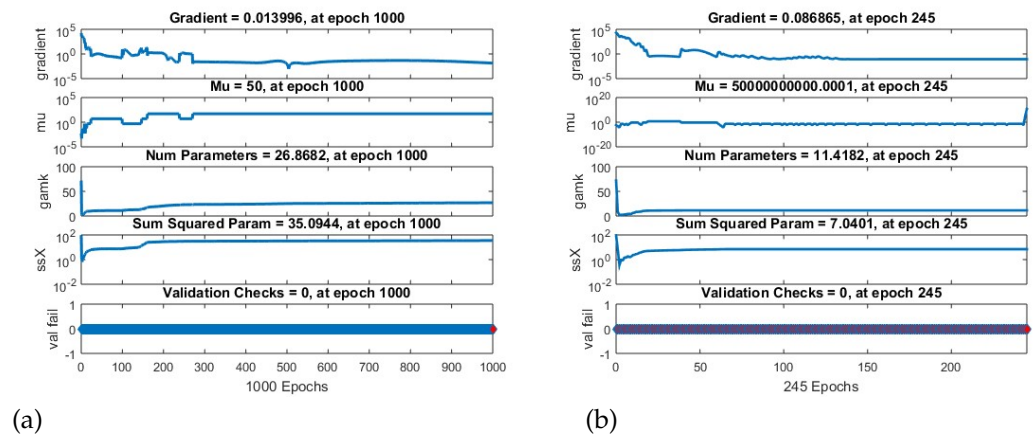
Figure 10. *Cont.*
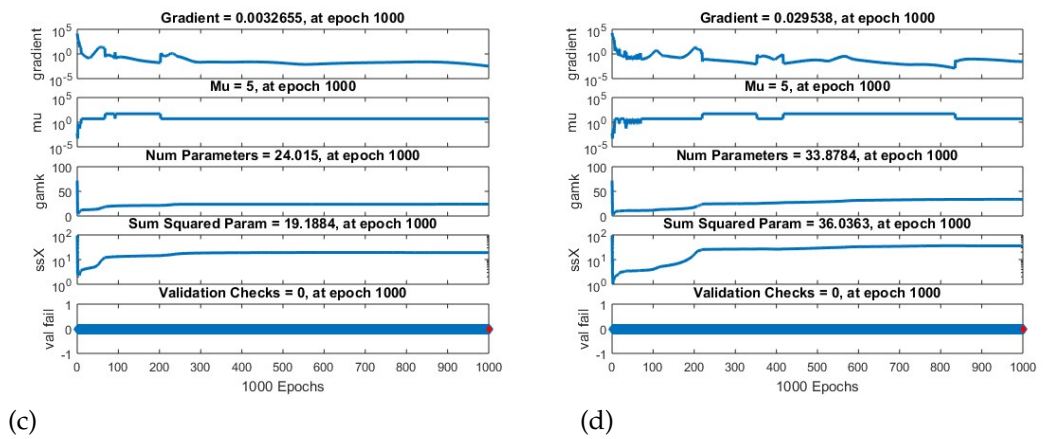
Figure 10. (**a**–**d**) Graphical view for illustration of training state for ANN-BR outcomes.
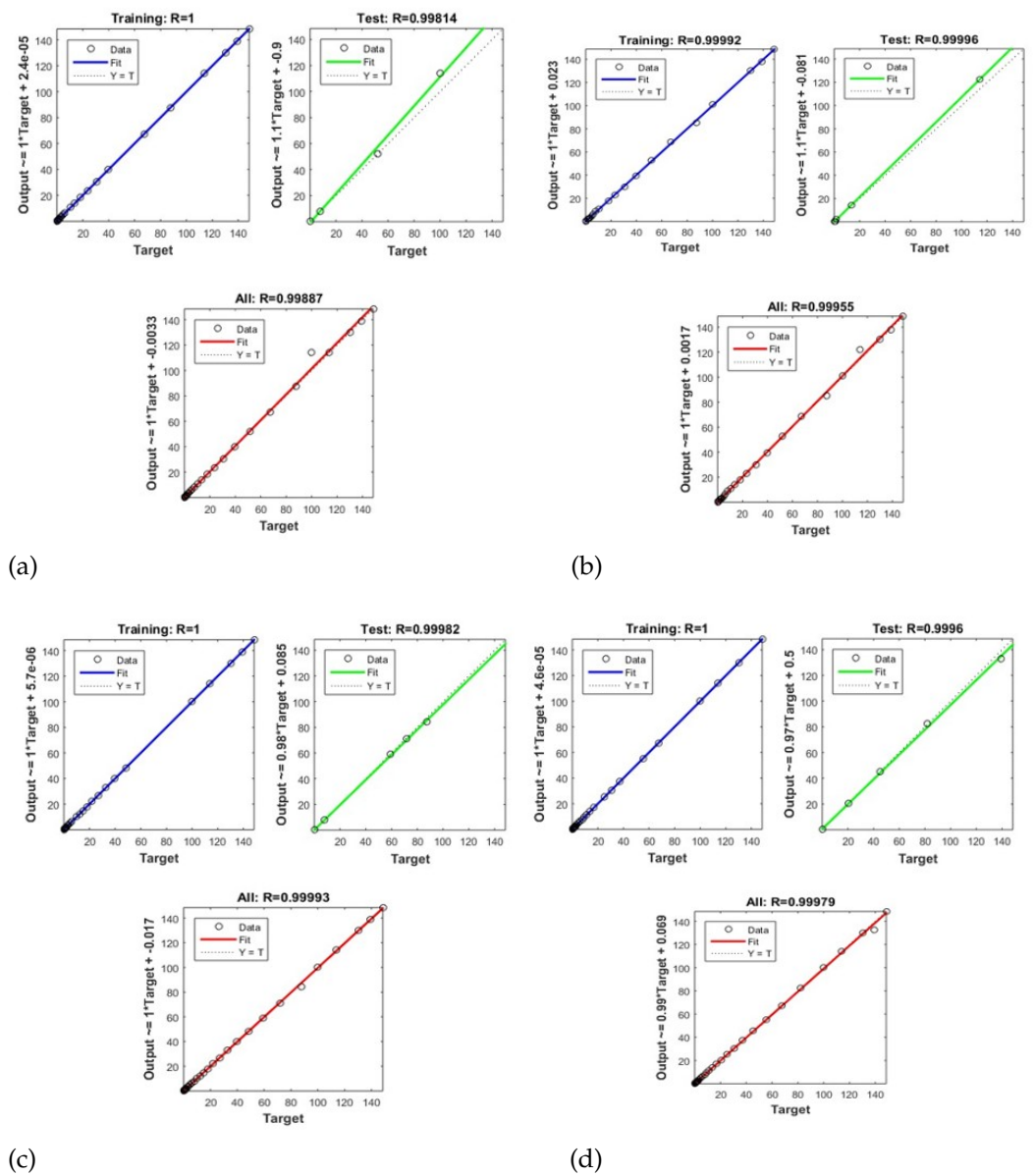
Figure 11. (**a**–**d**) Graphical view for illustration of regression performance for ANN-BR outcomes.
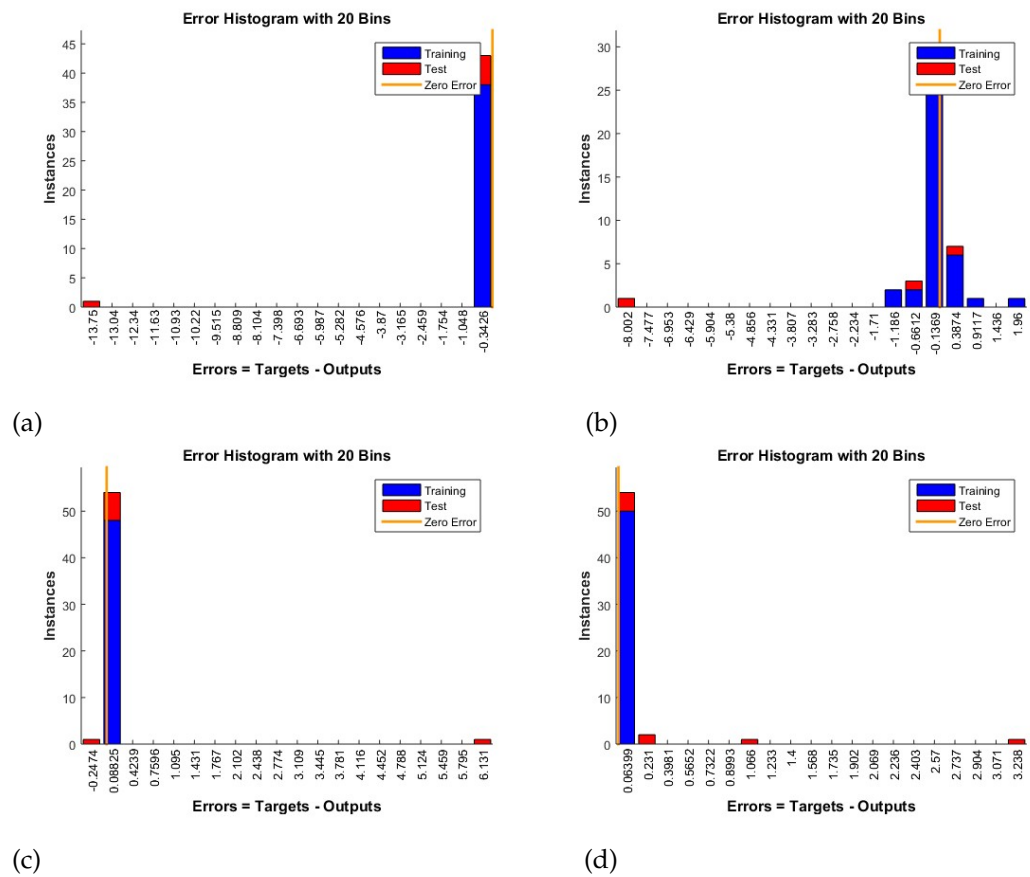
Figure 12. (**a**–**d**) Graphical view for illustration of error histogram for ANN-BR outcomes.
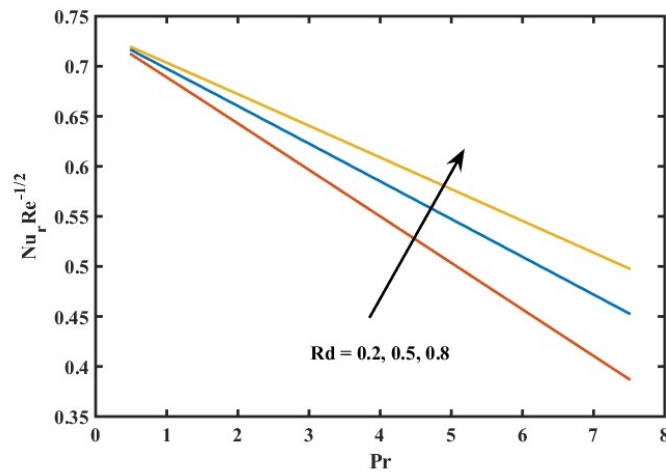
Figure 13. $Nu_r Re^{-\frac{1}{2}}$ with Pr.

7. Conclusions

An understanding of the effects of a Hall current and thermal radiation on the temporal variation of hybrid nanofluid flow over a disk surface would be useful in the advancement of thermal energy management and fluid dynamics using artificial intelligence and computational optimizing myths such as neural networks and Bayesian processes. The Hall current from the intervention of the magnetic field induces a Lorentz force, which alters the velocity and temperature profile of the electrically conducting nanofluid. This interaction helps enhance the ability to handle heat transfer actions and the flow of fluids. When a flow is complex and it occurs over a disk, thermal radiation happens through the rotation

of fluids and helps in cooling the system more and keeping the temperature levels fairly constant. Finally, ANN-BRs are used on the reference data set to estimate the approximate solutions of the hybrid nanofluid models.

- The obtained outcome proved that there was an increase in the both radial and azimuthal velocity distribution for the Hall current number.
- In the case of the development of the external magnetic field consequences, radial components diminished while the azimuthal velocity was lesser.
- An increase in heat transfer rate for M, R_d, and Q_E and a reduction in heat transfer rate for Pr, E_c, and m occurred.
- The slip parameter increased the temperature distribution accompanied by the up-surge.
- Heat transfer rate to a rotating disk can be accurately regulated with the help of volume fractions ϕ_1 and ϕ_2 of energy-carrying nanoparticles.
- There are certain implications when involving thermal radiation and a Hall current in the design and optimization of systems that involve hybrid nanofluids. Such understanding can be useful in a range of industries, such as aerospace and automotive engineering and renewable energy systems.

Nomenclature

u,v,w	Velocity components m.s^{-2}	τ_e	Electron collision time
z, ϕ, r	Polar coordinates	σ	Electric conductivity of Sm^{-1}
ν	Kinematic viscosity m^2.s^{-1}	T	Fluid temperature (K)
B_0	Magnetic field strength N.m.A^{-1}	M	Magnetic field number
μ	Dynamic viscosity kg.m^{-1}.s^{-1}	S	Unsteadiness parameter
c_p	Specific heat capacity J.K^{-1}.kg^{-1}	Ω	Disk rotating rate
θ	Dimensionless parameter	b	Positive constant
q_r	Radiative heat flux W.m^{-2}	c	Stretching rate
g	Swirling velocity flow	T_0	Origin temperature
f'	Axial velocity flow	T_{ref}	Constant reference temperature
f	Radial velocity flow	p_e	Electron pressure
ϕ_1	Volume fraction of CoFe$_2$O$_4$	n_e	Value of density of electrons
ϕ_2	Volume fraction of Al$_2$O$_3$	m	Hall current parameter
T_s	Surface temperature	μ_e	Magnetic permeability
ω_e	Cyclotron frequency of electrons	Sc	Schmidt parameter
Rd	Radiation parameter	Pr	Prandtl parameter
τ	Heat capacity ratio	D_T	Thermophoresis coefficient m^2.s^{-1}
Nu_r	Nusselt number	Q_E	Heat source/sink number
N_b	Brownian motion	D_B	mass diffusivity m^2.s^{-1}
ω	Rotating parameter	Sh_r	Sherwood number
N_t	Thermophoresis number	C	Fluid cenentration
ρ	Density of fluid kg.m^{-3}	c_p	Specific heat capacity J.K^{-1}.kg^{-1}
J	Current density	Ec	Eckert number

References

1. Okonkwo, E.C.; Wole-Osho, I.; Kavaz, D.; Abid, M. Comparison of experimental and theoretical methods of obtaining the thermal properties of alumina/iron mono and hybrid nanofluids. *J. Mol. Liq.* **2019**, *292*, 111377. [CrossRef]
2. Liu, X.; Wang, Z.; Gao, Q.; Sun, X.; Yang, Q.; Yang, H. Field synergy analysis of heat transfer characteristics of mixed nanofluid flow in self-excited oscillating heat exchanger tubes. *J. Therm. Anal. Calorim.* **2024**, *149*, 4893–4912. [CrossRef]
3. Rahman, S.I.; Moghassemi, A.; Arsalan, A.; Timilsina, L.; Chamarthi, P.K.; Papari, B.; Ozkan, G.; Edrington, C.S. Emerging trends and challenges in thermal management of power electronic converters: A state of the art review. *IEEE Access* **2024**, *12*, 50633–50672. [CrossRef]
4. Maghrabie, H.M.; Olabi, A.; Sayed, E.T.; Wilberforce, T.; Elsaid, K.; Doranehgard, M.H.; Abdelkareem, M.A. Microchannel heat sinks with nanofluids for cooling electronic components: Performance enhancement, challenges, and limitations. *Therm. Sci. Eng. Prog.* **2023**, *37*, 101608. [CrossRef]
5. Alshuhail, L.A.; Shaik, F.; Sundar, L.S. Thermal efficiency enhancement of mono and hybrid nanofluids in solar thermal applications–A review. *Alex. Eng. J.* **2023**, *68*, 365–404. [CrossRef]
6. Huminic, G.; Huminic, A. Capabilities of advanced heat transfer fluids on the performance of flat plate solar collector. *Energy Rep.* **2024**, *11*, 1945–1958. [CrossRef]
7. Kumar, S.; Kumar, R.; Thakur, R.; Kumar, S.; Lee, D. Effects of climate variables and nanofluid-based cooling on the efficiency of a liquid spectrum filter-based concentrated photovoltaic thermal system. *J. Therm. Anal. Calorim.* **2024**, *149*, 2273–2291. [CrossRef]
8. Wang, X.; Song, Y.; Li, C.; Zhang, Y.; Ali, H.M.; Sharma, S.; Li, R.; Yang, M.; Gao, T.; Liu, M.; et al. Nanofluids application in machining: A comprehensive review. *Int. J. Adv. Manuf. Technol.* **2024**, *131*, 3113–3164. [CrossRef]
9. Piazza, R. Thermophoresis: Moving particles with thermal gradients. *Soft Matter* **2008**, *4*, 1740–1744. [CrossRef]
10. Hafeez, A.; Khan, M.; Ahmed, J. Oldroyd-B fluid flow over a rotating disk subject to Soret–Dufour effects and thermophoresis particle deposition. *Proc. Inst. Mech. Eng. Part C J. Mech. Eng. Sci.* **2021**, *235*, 2408–2415. [CrossRef]
11. Chen, J.; Gao, P.; Gu, H.; Chen, Y.; Xinnuo, E.; Yu, J. Experimental study of the natural deposition of submicron aerosols on the surface of a vertical circular tube with non-condensable gases. *Nucl. Eng. Des.* **2024**, *417*, 112863. [CrossRef]
12. Karthik, K.; JK, M.; Kiran, S.; KV, N.; Prasannakumara, B.; Fehmi, G. Impacts of thermophoretic deposition and thermal radiation on heat and mass transfer analysis of ternary nanofluid flow across a wedge. *Int. J. Model. Simul.* **2024**, 1–13. . [CrossRef]
13. Goudarzi, S.; Shekaramiz, M.; Omidvar, A.; Golab, E.; Karimipour, A.; Karimipour, A. Nanoparticles migration due to thermophoresis and Brownian motion and its impact on Ag-MgO/Water hybrid nanofluid natural convection. *Powder Technol.* **2020**, *375*, 493–503. [CrossRef]
14. Daneshfar, R.; Soulgani, B.S.; Ashoori, S. Identifying the mechanisms behind the stability of silica nano-and micro-particles: Effects of particle size, electrolyte concentration and type of ionic species. *J. Mol. Liq.* **2024**, *397*, 124059. [CrossRef]
15. Shevchuk, I.V. *Modelling of Convective Heat and Mass Transfer in Rotating Flows*; Springer: Berlin/Heidelberg, Germany, 2016.
16. Tassaddiq, A.; Khan, S.; Bilal, M.; Gul, T.; Mukhtar, S.; Shah, Z.; Bonyah, E. Heat and mass transfer together with hybrid nanofluid flow over a rotating disk. *AIP Adv.* **2020**, *10*, 055317. [CrossRef]
17. Ahmed, J.; Nazir, F.; Fadhl, B.M.; Makhdoum, B.M.; Mahmoud, Z.; Mohamed, A.; Khan, I. Magneto-bioconvection flow of Casson nanofluid configured by a rotating disk in the presence of gyrotatic microorganisms and Joule heating. *Heliyon* **2023**, *9*, e18028. [CrossRef]
18. Saukani, I.; Nuraini, E.; Nurhadi, S.; Sumarno, A.S.H.; Saptawati, R.T.T.; Prasetyo, P.; Ms, F.I.S. Format Methods on Storage Media (Hard Disk) for Optimization Data Storage Capacity. *Asian J. Sci. Eng.* **2023**, *2*, 126–132. [CrossRef]
19. Mehmood, T.; Ramzan, M.; Howari, F.; Kadry, S.; Chu, Y.M. Application of response surface methodology on the nanofluid flow over a rotating disk with autocatalytic chemical reaction and entropy generation optimization. *Sci. Rep.* **2021**, *11*, 4021. [CrossRef]
20. Basit, M.A.; Farooq, U.; Imran, M.; Fatima, N.; Alhushaybari, A.; Noreen, S.; Eldin, S.M.; Akgül, A. Comprehensive investigations of (Au-Ag/Blood and Cu-Fe3O4/Blood) hybrid nanofluid over two rotating disks: Numerical and computational approach. *Alex. Eng. J.* **2023**, *72*, 19–36. [CrossRef]
21. Hussain, S.; Ali, A.; Rasheed, K.; Pasha, A.A.; Algarni, S.; Alqahtani, T.; Irshad, K. Application of response surface methodology to optimize MHD nanofluid flow over a rotating disk with thermal radiation and joule heating. *Case Stud. Therm. Eng.* **2023**, *52*, 103715. [CrossRef]
22. Yu, B.; Hu, H.; Li, J.; Ding, X.; Li, Z. Wetting-Enabled Microfluidic Surface for Fluid/Droplet Manipulation: Fabrication, Strategies and Applications. *Adv. Eng. Mater.* **2024**, *16*, 2400200. [CrossRef]
23. Wang, D.; Joshi, A.; Fan, L.S. Chemical looping technology—A manifestation of a novel fluidization and fluid-particle system for CO_2 capture and clean energy conversions. *Powder Technol.* **2022**, *409*, 117814. [CrossRef]
24. Khan, H.; Yaseen, M.; Rawat, S.K.; Khan, A. Insight into the significance of ternary hybrid nanofluid flow between two rotating disks in the presence of gyrotactic microorganisms. *Nano* **2024**. [CrossRef]
25. Guo, P.; Leng, Y.; Nazir, F.; Ahmed, J.; Mohamed, A.; Khan, I.; Elseesy, I.E. Mixed convection phenomenon for hybrid nanofluid flow exterior to a vertical spinning cylinder with binary chemical reaction and activation energy. *Case Stud. Therm. Eng.* **2024**, *54*, 103943. [CrossRef]
26. Averyanov, Y. Designing and Analyzing New Early Stopping Rules for Saving Computational Resources. Ph.D. Thesis, Lille, France, Inria, Le Chesnay-Rocquencourt, France, 2020.

27. Zaheer, K.; Saeed, S.; Tariq, S. Prediction of aerosol optical depth over Pakistan using novel hybrid machine learning model. *Acta Geophys.* **2023**, *71*, 2009–2029. [CrossRef]

28. Sharma, B.K.; Sharma, P.; Mishra, N.K.; Fernandez-Gamiz, U. Darcy-Forchheimer hybrid nanofluid flow over the rotating Riga disk in the presence of chemical reaction: Artificial neural network approach. *Alex. Eng. J.* **2023**, *76*, 101–130. [CrossRef]

29. Junaid, M.S.; Aslam, M.N.; Khan, M.A.; Saleem, S.; Riaz, M.B. Thermal analysis of a viscoelastic Maxwell hybrid nanofluid with graphene and polythiophene nanoparticles: Insights from an artificial neural network model. *Alex. Eng. J.* **2024**, *94*, 193–211. [CrossRef]

30. Alawi, O.A.; Kamar, H.M.; Shawkat, M.M.; Al-Ani, M.M.; Mohammed, H.A.; Homod, R.Z.; Wahid, M.A. Artificial intelligence-based viscosity prediction of polyalphaolefin-boron nitride nanofluids. *Int. J. Hydromechatron.* **2024**, *7*, 89–112. [CrossRef]

31. Freidberg, J.P. *Plasma Physics and Fusion Energy*; Cambridge University Press: Cambridge, UK, 2007.

32. Ahmed, J.; Gunaime, N.M.; Nazir, F. Thermal transport of magnetized hybrid nanofluid swirling over a disk surface with Hall current and thermal radiation effects. *Numer. Heat Transf. Part A Appl.* **2023**, 1–16. [CrossRef]

33. Abbasi, F.; Gul, M.; Shehzad, S. Hall effects on peristalsis of boron nitride-ethylene glycol nanofluid with temperature dependent thermal conductivity. *Phys. E Low-Dimens. Syst. Nanostructures* **2018**, *99*, 275–284. [CrossRef]

34. Khan, M.; Ahmed, J.; Ahmad, L. Chemically reactive and radiative von Kármán swirling flow due to a rotating disk. *Appl. Math. Mech.* **2018**, *39*, 1295–1310. [CrossRef]

35. Khan, M.; Ahmed, J.; Ahmad, L. Application of modified Fourier law in von Kármán swirling flow of Maxwell fluid with chemically reactive species. *J. Braz. Soc. Mech. Sci. Eng.* **2018**, *40*, 573. [CrossRef]

36. Aly, E.H.; Pop, I. MHD flow and heat transfer over a permeable stretching/shrinking sheet in a hybrid nanofluid with a convective boundary condition. *Int. J. Numer. Methods Heat Fluid Flow* **2019**, *29*, 3012–3038. [CrossRef]

37. Khashi'ie, N.S.; Waini, I.; Zainal, N.A.; Hamzah, K.; Arifin, N.M.; Pop, I. Multiple solutions and stability analysis of magnetic hybrid nanofluid flow over a rotating disk with heat generation. *J. Adv. Res. Fluid Mech. Therm. Sci.* **2023**, *102*, 59–72.

38. MacKay, D.J. Bayesian methods for backpropagation networks. In *Models of Neural Networks III: Association, Generalization, and Representation*; Springer: Berlin/Heidelberg, Germany, 1996; pp. 211–254.

39. Burden, F.; Winkler, D. Bayesian regularization of neural networks. In *Artificial Neural Networks: Methods and Applications*; Humana Press: Totowa, NJ, USA, 2009; pp. 23–42.